Supplementary Information for

# Hydroclimatic variability in Southeast Asia over the past two millennia

**Jessica K. Wang, Kathleen R. Johnson, Andrea Borsato, Dillon J. Amaya, Michael L. Griffiths, Gideon M. Henderson, Silvia Frisia, Andrew Mason**

Corresponding author: Kathleen R. Johnson
Email: Kathleen.johnson@uci.edu

**This PDF file includes:**

## Supplementary Text

### Cave setting and speleothem sample

Tham Doun Mai cave (TM cave) is a ~3,745 m-long cave located at ca. 352 m above sea level, adjacent to the Nam Ou river in Luang Prabang Province, Laos (20°45'N, 102°39'E). TM cave was extensively surveyed by members of the Northern Lao-European Cave Project in 2012 (Dreybrodt et al., 2013) and has only a single small (1.5 x 2 m) known entrance. The main portions of the cave are separated from a smaller entrance chamber by a short narrow crawl. The cave is formed in a Late Paleozoic limestone karst massif that rises several hundred meters above the river level. The overlying terrain is extremely steep and difficult to access, so has not likely been impacted by anthropogenic factors, such as deforestation. The thickness of bedrock overlying the cave varies from a few meters close to the entrance up to hundreds of meters in the deepest sections.

Cave monitoring conducted at TM cave includes temperature (T), relative humidity (RH), drip rate, and $pCO_2$ measurements, as well as collection of drip water and modern calcite samples for geochemical analysis. Results indicate that the temperature in TM cave is ~22 °C (close to the expected mean surface temperature) and the RH is >95%. Drip rates measured at two sites using Stalagmate automated drip loggers show strong seasonality, with rapid increases in drip rate at the onset of the summer monsoon season, indicating a piston flow-like hydrologic response to rain events (Tooth and Fairchild, 2003). Cave air $pCO_2$ is ~600 ppm, though we have only made these measurements between January and March, so cannot rule out the possibility of seasonal changes in cave ventilation. The average $\delta^{18}O$ of drip water samples taken from several locations in the cave between December 2010 and March 2017 is -7.8 ± 0.9 ‰ (n = 67), close to the weighted annual mean precipitation $\delta^{18}O$ of -8.2 ‰ simulated for our site using the IsoGSM isotope enabled climate model (Yoshimura et al., 2008). This suggests a mixing/transit time of at least one year before the drip water reaches the cave. The average $\delta^{18}O$ of modern calcite grown by placing glass plates under active drips for a period of at least one year is -8.7 ± 0.3 (n=40), samples close to the plate center range between -9 and -9.5 ‰, within the range of the predicted equilibrium values (Kim and O'Neil, 1997).

Stalagmite TM-17 (Fig. 1) was collected on a steep slope approximately ~200 m from the entrance, ~half way down the 26 m drop from the upper level to the active river passage. TM-17 was no longer an active stalagmite when collected, so no monitoring was possible on this specific drip site, though drip water and modern calcite samples were collected from other nearby sites. The regular and constant morphology of the TM-17 stalagmite in the investigated topmost section suggests a slow and almost constant drip rate (Kaufmann, 2003), likely preventing the possible influence of differential kinetic fractionation on the $\delta^{13}C$ signal as a function of fluctuating drip rates (Mühlinghaus et al., 2009). Petrographic logging of TM-17 following the rationale in Frisia et al. (Frisia et al., 2000) and the methodology described in Frisia et al. (Frisia, 2015) show that it is primarily composed of columnar calcite, ranging from compact to porous. While speleothem $\delta^{18}O$ values could reflect occurrence of non-classical crystallization pathways, which include the precipitation of amorphous carbonate or vaterite (Demény et al., 2016), for TM-17 this effect is unlikely because *in situ* precipitation experiments from freshly collected dripwater near the TM-17 sampling site yielded exclusively calcite. By considering that crystallization processes and speleothem growth had a negligible effect in driving $\delta^{18}O$ changes and that any kinetic effects were relatively minor and constant, we assume

that TM-17 $\delta^{18}O$ variations are primarily driven by change in mean precipitation $\delta^{18}O$ and $\delta^{13}C$ variations are primarily driven by soil and vegetation responses to changing water balance.

**Spectral and Wavelet Analyses**

To detect decadal to centennial cycles in the TM-17 record, we performed a red-noise power spectral analysis (REDFIT) (Schulz and Mudelsee, 2002) specifically adapted for unevenly-spaced data (Fig. S3) using the PAST software (Hammer et al., 2001). The results highlight decadal to centennial-scale periodicities (193, 128, 29 and 9 years) in the TM-17 $\delta^{18}O$ record that are significant above a red-noise background of a first-order autoregressive process (Fig S2). Additional spectra performed from age models generated via Monte-Carlo simulations in the COPRA1.0 model (Breitenbach et al., 2012) also show significant multidecadal-centennial cycles thus confirming the robustness of the TM-17 $\delta^{18}O$ periodicities. Wavelet transform analysis (Torrence et al., 1998) of the $\delta^{18}O$ record also indicates significant multidecadal to centennial-scale variability throughout the record (Fig. S2). These observed periodicities may be associated with those of known solar cycles, such as the sub-harmonics of the de Vries-Suess (~210 years) (Stuiver et al., 1998) and the Hale (~132 years) (Attolini et al., 1990) solar cycles. However, we are cautious in interpreting the results from the spectra to suggest causation and cannot completely rule out the possible influence of internal coupled climate modes such as the ENSO (Zhao et al., 2015) or AMO (Berkelhammer et al., 2010). Power spectral analysis of the $\delta^{13}C$ data reveals periodicities centered at 386, 66-77, 37 years (significant at 95% confidence level) and these periodicities are supported by wavelet transform analysis (Fig. S2).

## Supplementary Methods

**Synchrotron radiation X-ray fluorescence.** Synchrotron radiation X-ray fluorescence (XRF) microscopy was performed on the XFM beamline at the Australian Synchrotron (Paterson et al., 2011) using the Kirkpatrick-Baez mirror microprobe end-station. A 12 mm-thick polished slab was analyzed with a monochromatic 2 μm beam spot size and energy at 18.5 keV. A 45 x 2 mm map was acquired in the axial part of the stalagmite at 2 μm pixel size resolution on both axis and a dwell time of 1.2 ms/pixel, yielding a detection limit for Sr of ~ 2 ppm. Single element foils Mn, Fe and Pt (Micromatter, Canada) were utilized as references to calibrate the final elemental spectra. The Maia XRF spectral data were analyzed using the GeoPIXE software suite which uses a fundamental parameters approach, with spectral deconvolution and imaging using the dynamic analysis method. Spectra were fitted using X-ray line relative intensities that reflect integration of yields and X-ray self-absorption effects for the calcite matrix and the contrasting efficiency characteristics across the detector array (Ryan et al., 2010).

**Age Model.** Annual laminae counting was conducted on the Sr synchrotron XRF map clustered at 4 μm resolution by visually identifying the Sr minima using ImageJ. The corrugated nature of the lamination and the presence of blurred areas centered along crystal boundaries prevented the use of automated laminae counting techniques. Two separate continuous counts were made following the areas with sharper definition on the map (Fig. 1), whereas in condensed and blurred intervals up to four different counts were made. The final laminae number was calculated with the arithmetic average on successive sections of the map. The total counting error, C, between replicate counts was 23 years, whereas an error of 54 years was estimated for the presence of fuzzy areas in which the lamination is not completely clear (F). The total laminae

counting error (LC) was calculated as: $LC = \sqrt{C^2 + F^2}$ (Domínguez-Villar et al., 2012). The calculated LC error of 58.7 years amounts to ~3% of the total layers counted (1,934).

Due to the fact that TM-17 was not active upon collection and the laminae counting age model is therefore floating, we anchored the laminae counting age model to the U-Th ages using a least-squares fit method (Domínguez-Villar et al., 2012). One U-Th age (TM-17 U3) was excluded during application of this method due to the large uncertainty on the raw age, which indicates a poor analysis. We determined the top age by calculating the linear regression of the relative laminae number versus the U-Th ages by using least squares fitting. The slope of the regression (0.98, with a 95% confidence range of 0.95 and 1.02) is indistinguishable from 1 and confirms the annual nature of the Sr laminae. The errors in the age model were constructed from the individual U-Th 2σ error bars by propagating the calculated LC error of 3% within each section between two adjacent U-Th ages. Based on this method, the average age uncertainty throughout the record is 26 years. In summary, the final TM-17 chronology is constrained by the six uranium-thorium (U-Th) dates coupled with annual laminae in Sr measured using a least-squares fit method to the U-Th dates (Table S1 and Fig. 1).

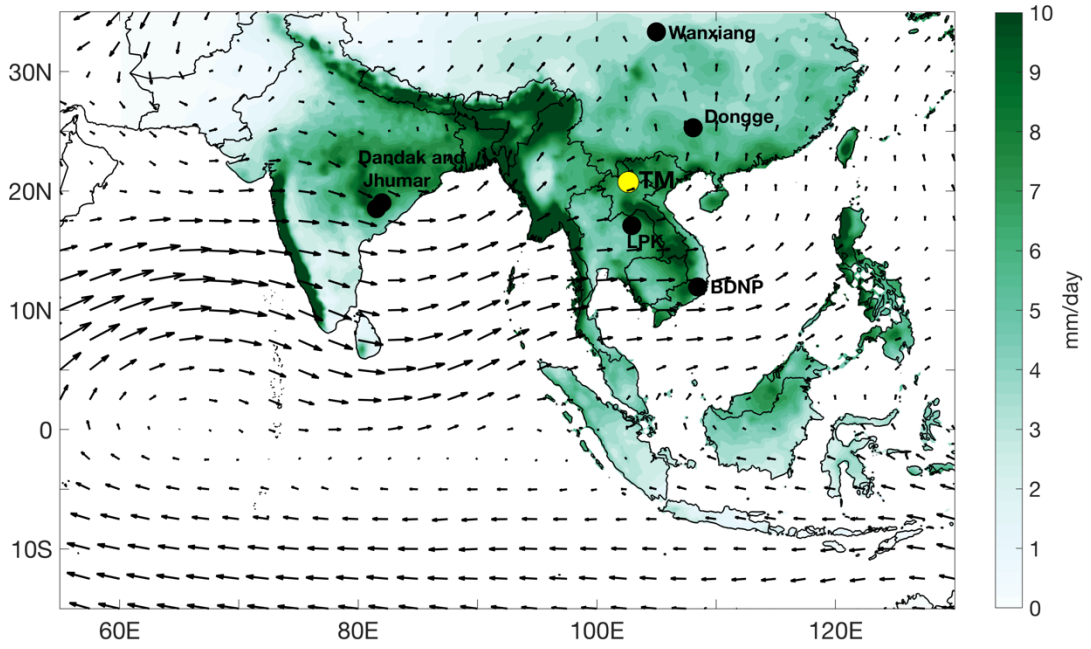


Fig S1. Summer (JJAS) precipitation and 850 mb winds climatology and location of select paleoclimate records. Mean JJAS precipitation (1951-2007 CE) derived from Asian Precipitation - Highly-Resolved Observational Data Integration Towards Evaluation (APHRODITE) (Yatagai et al., 2012). 850 mb winds are derived from NCEP Reanalysis mean (1951-2007 CE) (Kalnay et al., 1996). The location of Tham Doun Mai Cave, Laos is indicated by the yellow circle. The locations of select regional paleoclimate records marked by black circles. These include Wanxiang Cave, China (Zhang et al., 2008), Dongge Cave, China (Zhao et al., 2015), Dandak and Jhumar Caves, India (Sinha et al., 2007), Bidoup Nui Ba National Park (BDNP) in Southern Vietnam (Buckley et al., 2010), and Lake Pa Kho, Thailand (Chawchai et al., 2015; Yamoah et al., 2016).

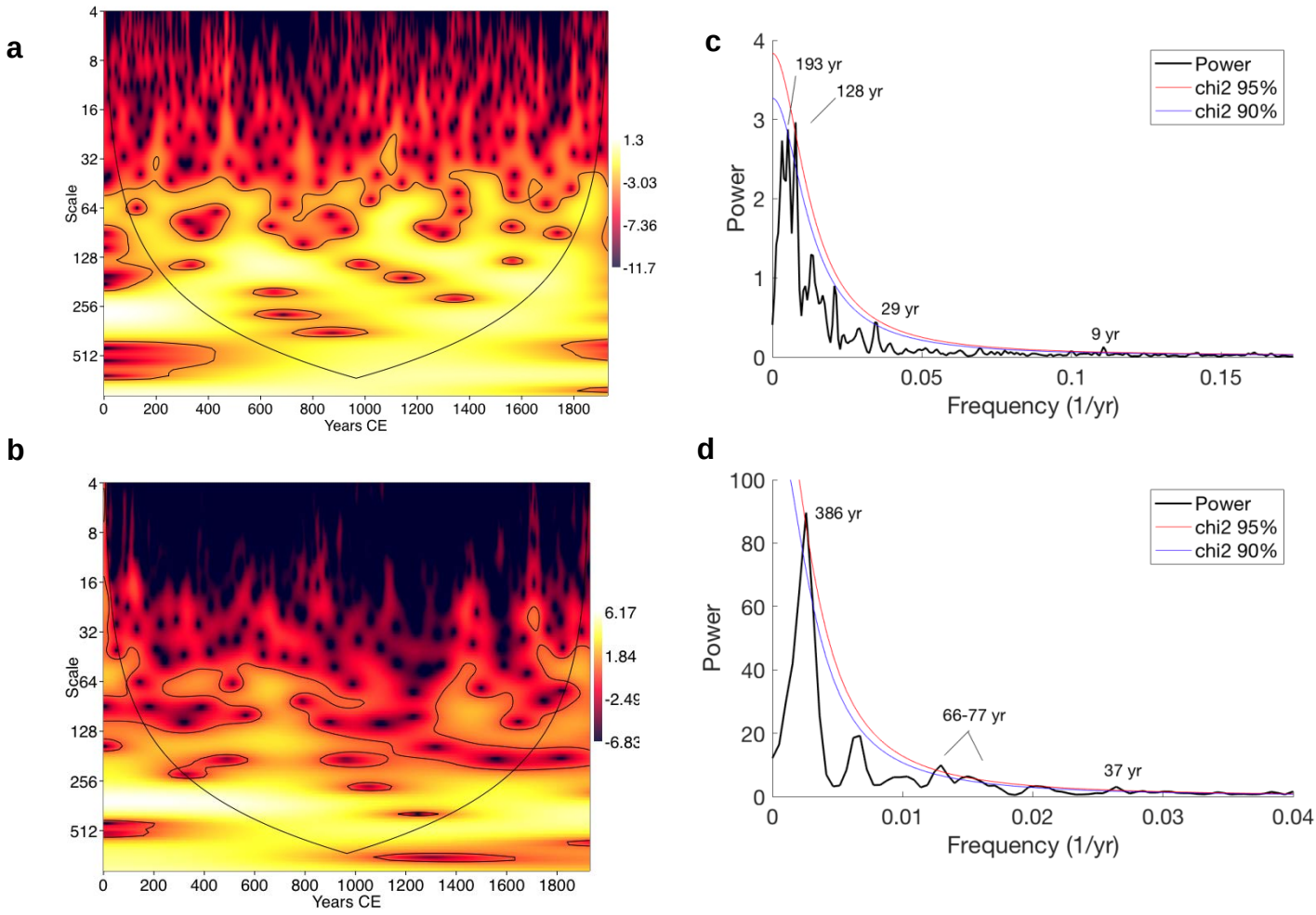


Fig. S2. Morlet wavelet analysis performed using the software PAST (Hammer et al., 2001) and the spectral analysis of TM-17 $\delta^{18}O$ and $\delta^{13}C$ performed with the REDFIT method (Schulz and Mudelsee, 2002). (a) $\delta^{18}O$ and (b) $\delta^{13}C$ wavelet transform from colors ranging from deep purple (weak) to bright yellow (strong). The TM-17 data were interpolated to a 2-year timescale using MATLAB interp1 function. Black lines indicate 95% significance level and the cone of influence. (c) $\delta^{18}O$ and (d) $\delta^{13}C$ spectral power performed by REDFIT (Schulz and Mudelsee, 2002), which uses the Lomb-Scargle Fourier Transform for unevenly spaced data. The black line indicates the power spectrum. The blue and red lines represent the 95% and 90% confidence limits, respectively, relative to the red-noise spectrum. The utilized parameters were window: welch; oversample: 2; segment: 4.

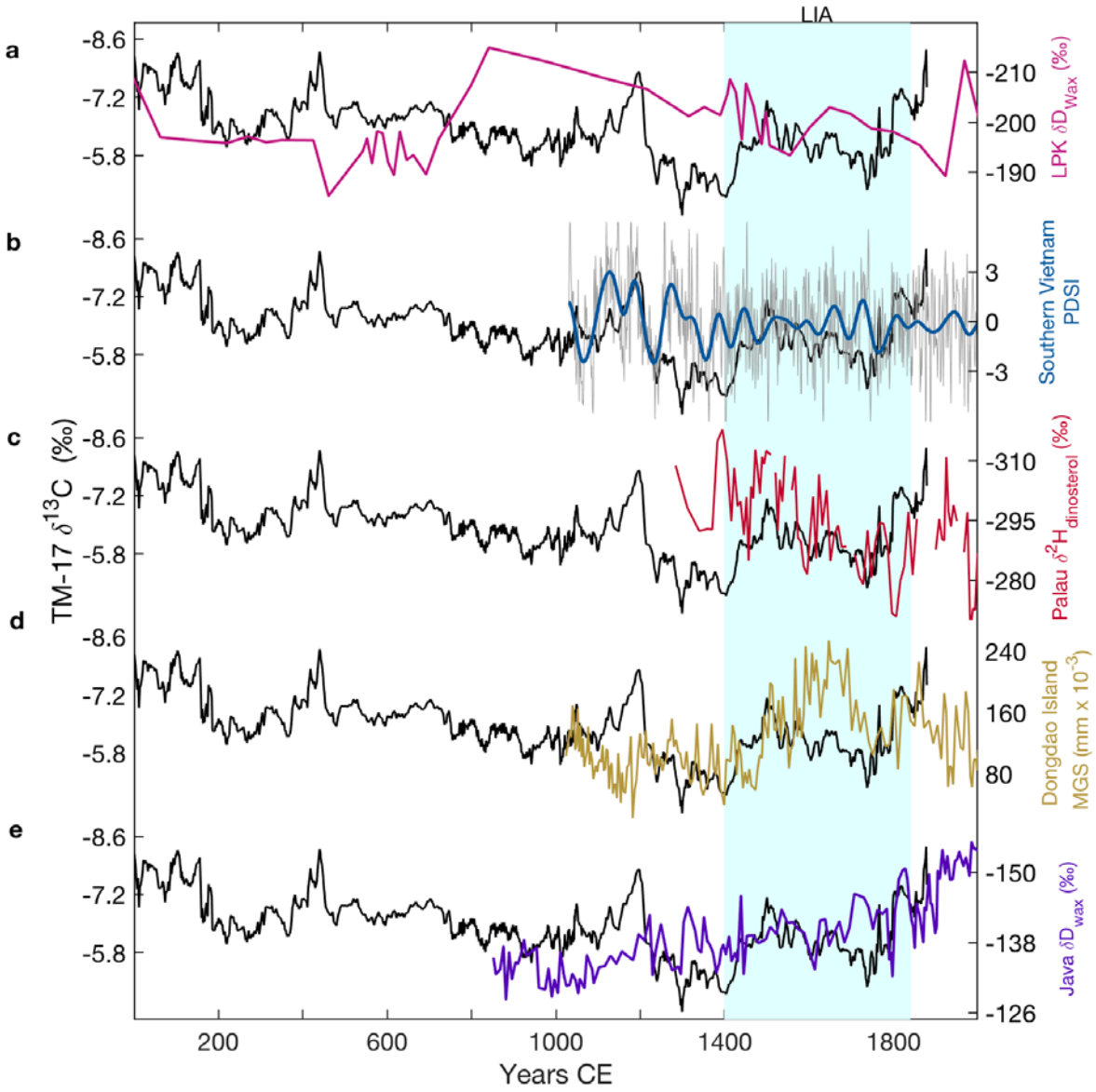


Figure S3. Comparison of the TM-17 $\delta^{13}C$ record with regional proxy records. The black line in all panels shows the stalagmite TM-17 $\delta^{13}C$ record compared with (a) Leaf wax ($\delta D_{wax}$) from Lake Pa Kho (LPK), Thailand (Chawchai et al., 2015; Yamoah et al., 2016). (b) Tree ring reconstructed Palmer Drought Severity Index (PDSI) from Bidoup Nui Ba National Park (BDNP), Vietnam (Buckley et al. 2010). The grey line represents the raw PDSI and the blue line is the 15-year Butterworth filtered data. (c) Dinosterol $\delta^{2}H$ from Clear Lake, Palau (Richey and Sachs, 2016). (d) Mean grain size (MGS) from Cattle Pond, Dongdao Island, South China Sea (Yan et al., 2011). (e) Leaf wax δD from Lake Lading, East Java, western Indonesia (Konecky et al., 2013). The y-axes in all panels are oriented such that wetter conditions/stronger convection is oriented up. Blue shaded bar corresponds to the timing of the Little Ice Age (LIA; 1400-1850).

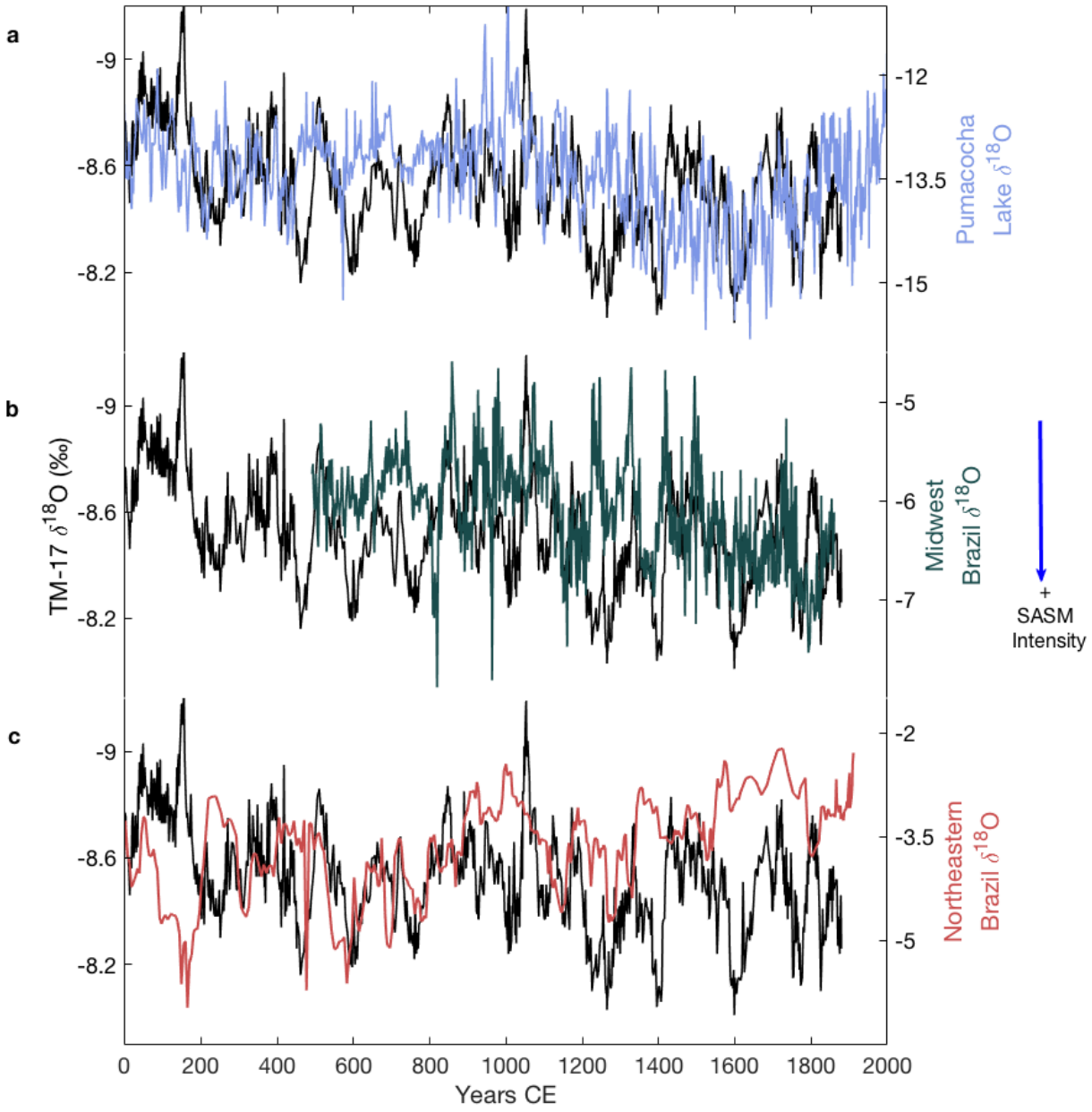


Figure S4. Comparison of the TM-17 record with South American Monsoon proxy records. The black line in all panels shows the stalagmite TM-17 $\delta^{18}O$ record compared with (a) Pumacocha Lake $\delta^{18}O$ (Bird et al., 2011). (b) Stalagmite $\delta^{18}O$ from Curupira Cave, Brazil (Novello et al., 2016). (c) Stalagmite $\delta^{18}O$ from Diva de Maura Cave, Brazil (Novello et al., 2012).The y-axes in all panels are oriented such that weaker monsoon intensity recorded at TM Cave and stronger South American summer monsoon intensity is down.

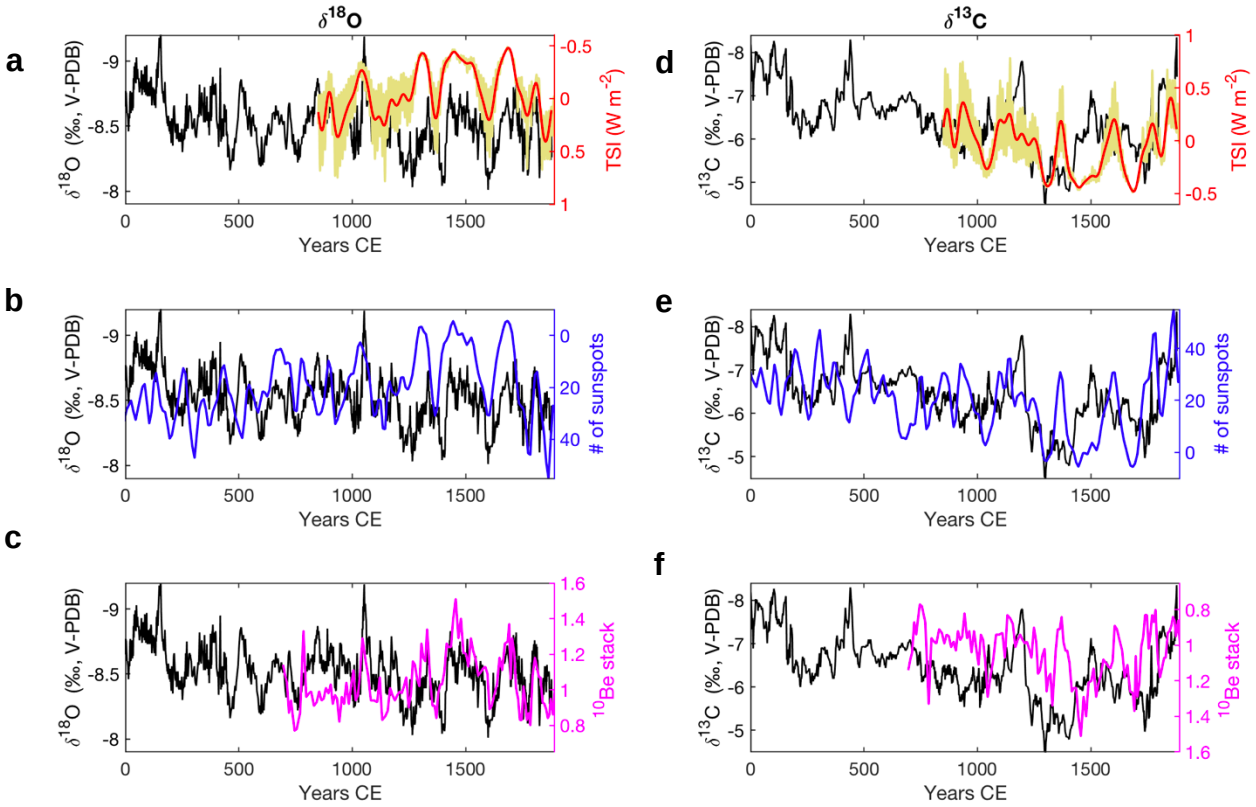


Fig. S5. Comparison of TM-17 $\delta^{18}O$ and solar activity proxies. (a-c) show the $\delta^{18}O$ record and (d-f) show the $\delta^{13}C$ record in black compared with records of (a) raw total solar irradiance reconstruction (Vieira et al., 2011) in yellow and 50-year low pass filtered time series in red, (b) reconstruction of the sunspot number based on $^{14}C$ concentrations (Solanki et al., 2004) in blue and (c) $^{10}Be$ stack derived from Central Antarctica ice cores in pink (Delaygue and Bard, 2011). The y-axes in (a-c) are oriented such that weaker monsoon intensity and increased solar activity are down. The y-axes in (d-f) are oriented such that drier conditions and decreased solar activity are down.

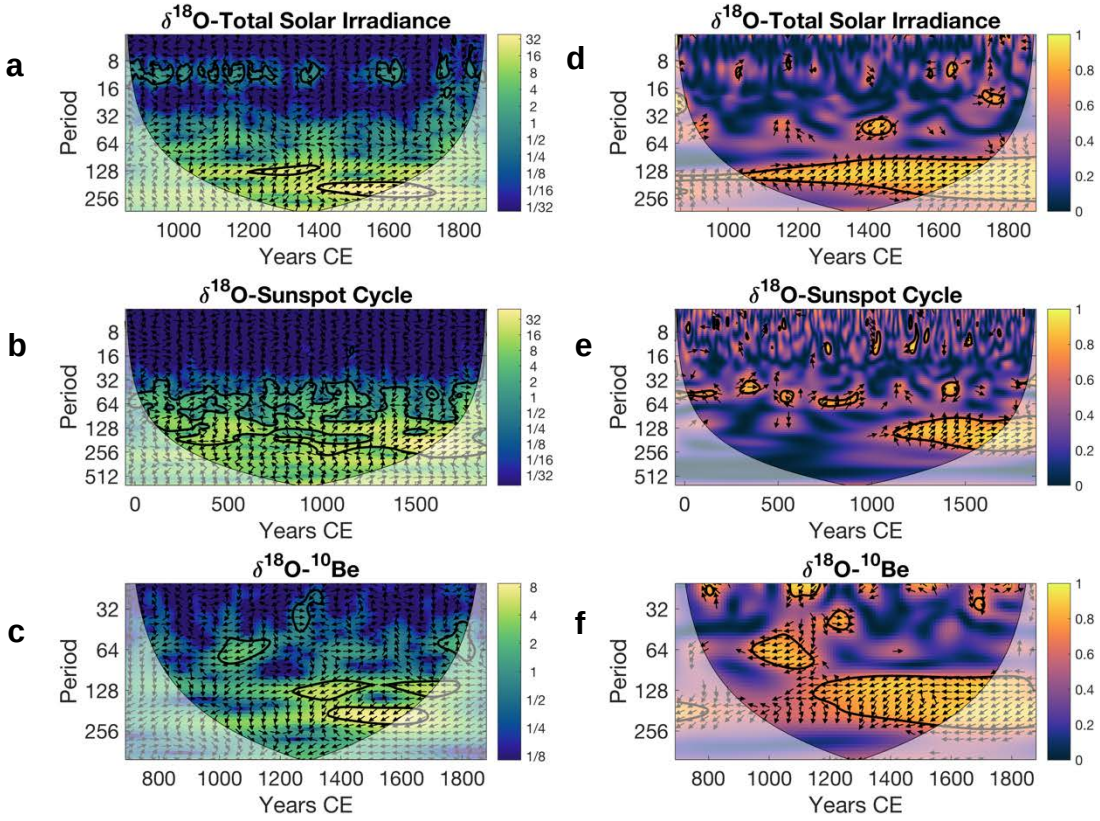


Fig. S6. Cross-wavelet and Wavelet Coherence analyses between TM-17 $\delta^{18}O$ with solar activity proxies. (a,d) Reconstructed Total Solar Irradiance reconstruction (Vieira et al., 2011). (b,e) Reconstruction of the sunspot number based on $^{14}C$ concentrations (Solanki et al., 2004). (e,f) $^{10}Be$ stack derived from Central Antarctica ice cores (Delaygue and Bard, 2011). For clarity, (a-c) are the cross-wavelet analyses and (e-f) are the wavelet coherence analyses. The cross-wavelet measures the high common power in time-frequency space and the wavelet coherence measures the linear correlation between two time series at a given frequency (Grinsted et al., 2004). In all of the panels, the black outlines represent significance at 95% confidence interval against a red noise backgrounds using Monte Carlo methods. Right-facing arrows represent relative in-phase between the time series. Arrows are pointing to the left (out of phase) in (c,f) given the inverse relationship between $^{10}Be$ and $\delta^{18}O$, but still reflects decreased solar activity corresponding to increased monsoon intensity. Thin black line and white shading represents the cone of influence. The results show significant cross-wavelet power and high coherency at the multidecadal-centennial timescales in all panels.

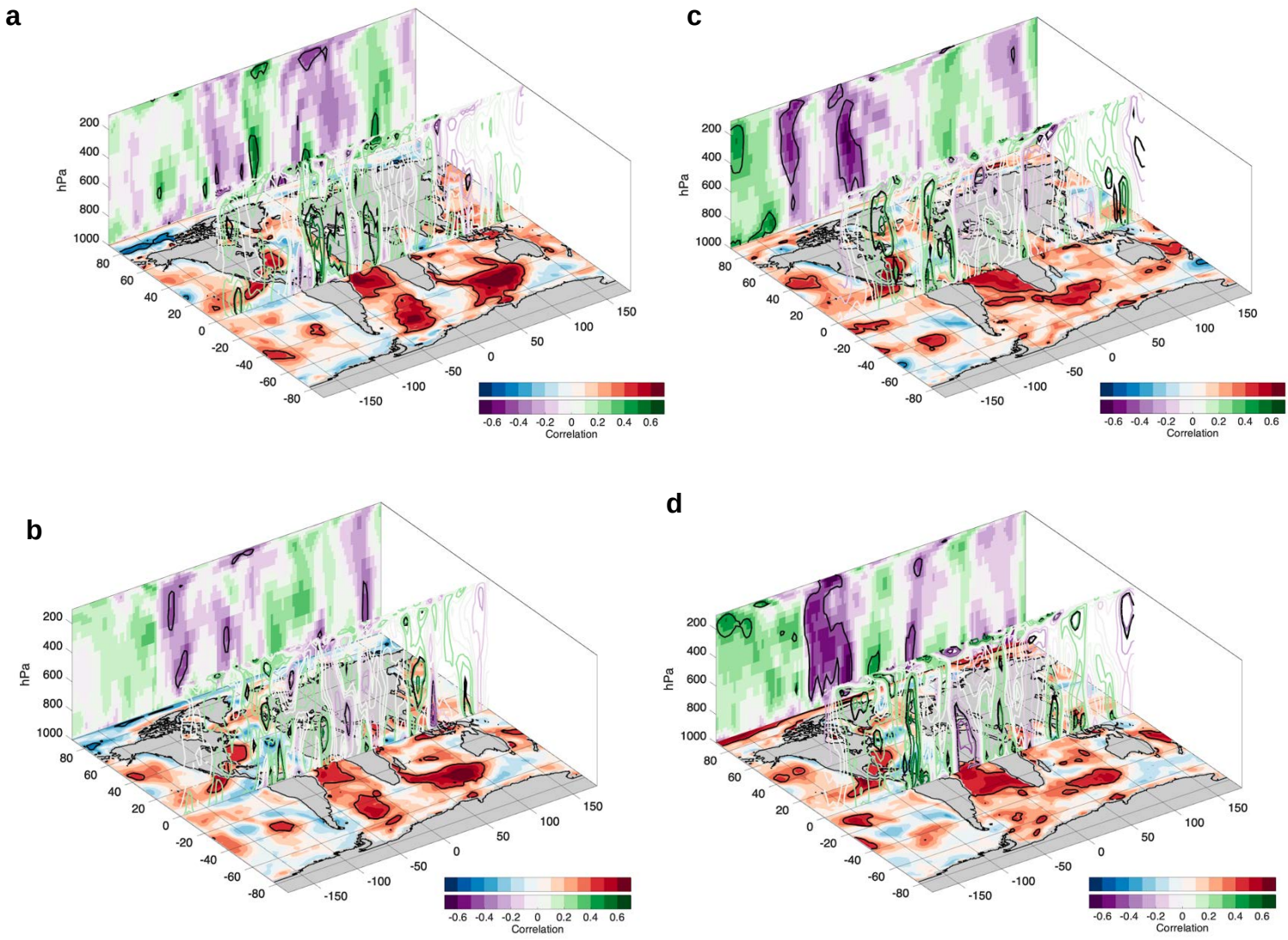


Fig. S7. As described in Fig. 4 except for each individual ensemble member in the CESM LME solar-only forcing. (a) Ensemble member 1 from CESM solar-only run. (b) Ensemble member 2 from solar-only run. (c) Ensemble member 3 from solar-only run. (d) Ensemble member 4 from solar-only run.

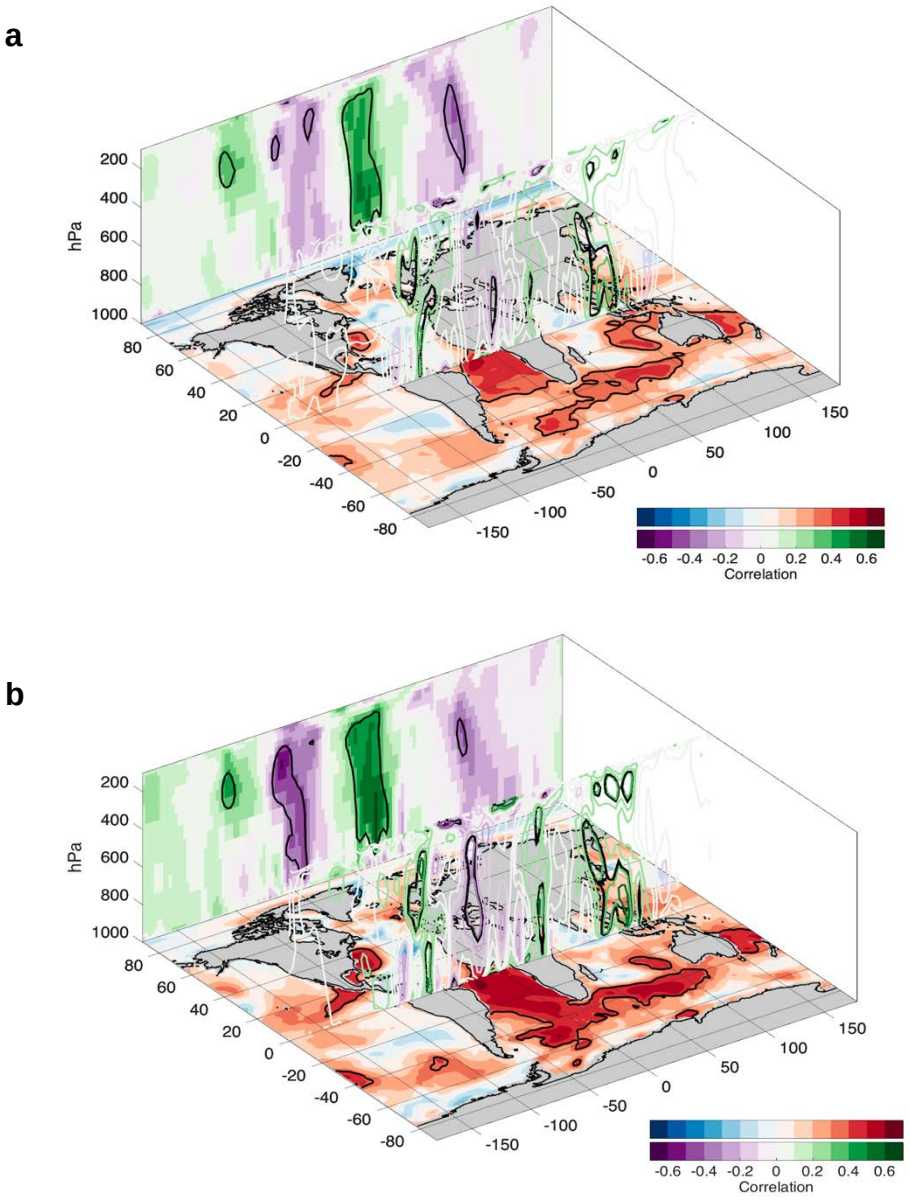


Fig. S8. As described in Fig. 4. (a) Solar-only forcing ensemble mean from 850-1878 CE. (b) Solar-only forcing ensemble mean from 1200-1878 CE.

**Table S1.** U-Th concentrations, isotope ratios, and calculated ages for TM-17. Uncertainties are 2σ. Half-lives are those of Cheng et al. (2013). All ages are relative to 1950 CE. Corrected ages assume the initial $^{230}Th/^{232}Th$ atomic ratio of 5.38 +5.38/-4.84 ppm. The activity ratios are indicated by parentheses. TM-17 U3 was excluded from the age model due to a large uncertainty.

| Sample ID | Depth from top (cm) | $^{238}U$ (ppm) | $^{232}Th$ (ppb) | $(^{234}U/^{238}U)$ | $(^{230}Th/^{232}Th)$ | $(^{230}Th/^{238}U)$ | $(^{234}U/^{238}U)_{initial}$ | Raw age (yrs BP) | Corr. age (yrs BP) |
|---|---|---|---|---|---|---|---|---|---|
| TM-17 U1 | 0.3 | 2.22 | 2.05 | 1.6844 ± 0.0065 | 16.0 ± 0.4 | 0.0048 ± 0.0001 | 1.6849 ± 0.0065 | 249 ± 7 | 229 ± 19 |
| TM-17 U27 | 0.9 | 1.88 | 0.92 | 1.6803 ± 0.0051 | 55.2 ± 1.4 | 0.0089 ± 0.0002 | 1.6810 ± 0.0050 | 511 ± 13 | 501 ± 16 |
| TM-17 U28 | 1.3 | 2.10 | 0.81 | 1.6747 ± 0.0052 | 90.9 ± 1.9 | 0.0116 ± 0.0002 | 1.6600 ± 0.0052 | 691 ± 14 | 682 ± 16 |
| TM-17 U29 | 1.8 | 1.95 | 1.17 | 1.6645 ± 0.0051 | 84.9 ± 1.2 | 0.0167 ± 0.0002 | 1.6660 ± 0.0052 | 1034 ± 13 | 1020 ± 18 |
| TM-17 U3 | 2.7 | 2.09 | 0.33 | 1.6521 ± 0.0051 | 469.3 ± 29.3 | 0.0245 ± 0.0007 | 1.6550 ± 0.0053 | 1563 ± 46 | 1560 ± 47 |
| TM-17 U30 | 3.3 | 2.89 | 0.27 | 1.6663 ± 0.0051 | 880.9 ± 26.2 | 0.0274 ± 0.0002 | 1.6700 ± 0.0051 | 1742 ± 13 | 1739 ± 13 |
| TM-17 U31 | 3.8 | 3.12 | 0.63 | 1.6663 ± 0.0051 | 460.3 ± 5.4 | 0.0303 ± 0.0002 | 1.6700 ± 0.0051 | 1932 ± 11 | 1927 ± 12 |

Uncertainties are 2σ. Half lives are those of Cheng et al., 2013. All ages are relative to 1950. Corrected ages assume the initial $^{230}Th/^{232}Th$ atomic ratio of 5.38 +5.38/-4.84 ppm. The activity ratios are indicated by the round brackets. TM-17 U3 was excluded from the age model due to a large uncertainty.

**Table S2.** Correlation coefficients reported between TM-17 $\delta^{18}O$ and solar activity proxies: Total Solar Irradiance (TSI) (Vieira et al., 2011), sunspot number (Solanki et al., 2004), and $^{10}Be$ stack (Delaygue and Bard, 2011). The Pearson *r* values are shown for both unfiltered (raw) and 50 year low-pass filtered data for two separate time periods: 850-1878 CE and 1200-1878 CE. The bolded coefficients are significant at 95% confidence level or greater. The numbers in the parenthesis represent the p-value calculated using the method of Macias-Fauria et al. (2012)[1].

| | | 850-1878 CE | 1200-1878 CE |
|---|---|---|---|
| **TSI** | Raw | 0.16 (0.31) | **0.42 (0.01)** |
| | 50-year lowpass filter | 0.21 (0.37) | **0.54 (0.01)** |
| **Sunspot Number** | Raw | 0.23 (0.27) | **0.48 (0.05)** |
| | 50-year lowpass filter | 0.24 (.029) | **0.52 (0.05)** |
| **$^{10}Be$** | Raw | -0.31 (0.12) | **-0.55 (< 0.01)** |
| | 50-year lowpass filter | -0.33 (0.14) | **-0.60 (< 0.01)** |

[1] Reported correlation coefficients are Pearson's *r* values, unless otherwise noted. Significance testing was conducted using a combination of 1,000 Monte Carlo iterations and time-series modelling in the frequency domain to consider the effect of serial correlation (Macias-Fauria et al., 2012).

## References


Attolini, M.R., Cecchini, S., Galli, M., Nanni, T., 1990. On the persistence of the 22 y solar cycle. Sol. Phys. 125, 389–398. https://doi.org/10.1007/bf00158414

Berkelhammer, M., Sinha, A., Mudelsee, M., Cheng, H., Edwards, R.L., Cannariato, K., 2010. Persistent multidecadal power of the Indian Summer Monsoon. Earth Planet. Sci. Lett. 290, 166–172. https://doi.org/10.1016/j.epsl.2009.12.017

Bird, B.W., Abbott, M.B., Vuille, M., Rodbell, D.T., Stansell, N.D., Rosenmeier, M.F., 2011. A 2,300-year-long annually resolved record of the South American summer monsoon from the Peruvian Andes. Proc. Natl. Acad. Sci. U. S. A. 108, 8583–8. https://doi.org/10.1073/pnas.1003719108

Breitenbach, S.F.M., Rehfeld, K., Goswami, B., L Baldini, J.U., Ridley, H.E., Kennett, D.J., Prufer, K.M., Aquino, V. V, Asmerom, Y., Polyak, V.J., Cheng, H., Kurths, J., Marwan, N., 2012. Climate of the Past COnstructing Proxy Records from Age models (COPRA) 8, 1765–1779. https://doi.org/10.5194/cp-8-1765-2012

Buckley, B.M., Anchukaitis, K.J., Penny, D., Fletcher, R., Cook, E.R., Sano, M., Nam, L.C., Wichienkeeo, A., Minh, T.T., Hong, T.M., 2010. Climate as a contributing factor in the demise of Angkor, Cambodia. Proc. Natl. Acad. Sci. U. S. A. 107, 6748–52. https://doi.org/10.1073/pnas.0910827107

Chawchai, S., Chabangborn, A., Fritz, S., Väliranta, M., Mörth, C.-M., Blaauw, M., Reimer, P.J., Krusic, P.J., Löwemark, L., Wohlfarth, B., 2015. Hydroclimatic shifts in northeast Thailand during the last two millennia – the record of Lake Pa Kho. Quat. Sci. Rev. 111, 62–71. https://doi.org/10.1016/j.quascirev.2015.01.007

Cheng, H., Lawrence Edwards, R., Shen, C.-C., Polyak, V.J., Asmerom, Y., Woodhead, J., Hellstrom, J., Wang, Y., Kong, X., Spötl, C., Wang, X., Calvin Alexander, E., 2013. Improvements in 230Th dating, 230Th and 234U half-life values, and U–Th isotopic measurements by multi-collector inductively coupled plasma mass spectrometry. Earth Planet. Sci. Lett. 371–372, 82–91. https://doi.org/10.1016/j.epsl.2013.04.006

Delaygue, G., Bard, E., 2011. An Antarctic view of Beryllium-10 and solar activity for the past millennium. Clim. Dyn. 36, 2201–2218. https://doi.org/10.1007/s00382-010-0795-1

Demény, A., Németh, P., Czuppon, G., Leél-Őssy, S., Szabó, M., Judik, K., Németh, T., Stieber, J., 2016. Formation of amorphous calcium carbonate in caves and its implications for speleothem research. Sci. Rep. 6, 39602. https://doi.org/10.1038/srep39602

Domínguez-Villar, D., Baker, A., Fairchild, I.J., Edwards, R.L., 2012. A method to anchor floating chronologies in annually laminated speleothems with U–Th dates. Quat. Geochronol. 14, 57–66. https://doi.org/10.1016/J.QUAGEO.2012.04.019

Dreybrodt, J., Laumanns, M., Steiner, H., 2013. Ten years of exploration and over 100km of caves surveyed in Northern Laos, in: UIS Congress Brno. pp. 68–70.

Frisia, S., 2015. Microstratigraphic logging of calcite fabrics in speleothems as tool for palaeoclimate studies. Int. J. Speleol. 1, 1–16. https://doi.org/10.5038/1827-806X.44.1.1

Frisia, S., Borsato, A., Fairchild, I.J., McDermott, F., 2000. Calcite Fabrics, Growth Mechanisms, and Environments of Formation in Speleothems from the Italian Alps and Southwestern Ireland. J. Sediment. Res. 70, 1183–1196. https://doi.org/10.1306/022900701183

Grinsted, A., Moore, J.C., Jevrejeva, S., 2004. Nonlinear Processes in Geophysics Application of the cross wavelet transform and wavelet coherence to geophysical time series. Nonlinear

Process. Geophys. 11, 561–566.
Hammer, Ø., Harper, D.A.T., Ryan, P.D., 2001. PAST: Paleontological statistics software package for education and data analysis. 9pp. 4, 9.
Kalnay, E., Kanamitsu, M., Kistler, R., Collins, W., Deaven, D., Gandin, L., Iredell, M., Saha, S., White, G., Woollen, J., Zhu, Y., Leetmaa, A., Reynolds, R., Chelliah, M., Ebisuzaki, W., Higgins, W., Janowiak, J., Mo, K.C., Ropelewski, C., Wang, J., Jenne, R., Joseph, D., Kalnay, E., Kanamitsu, M., Kistler, R., Collins, W., Deaven, D., Gandin, L., Iredell, M., Saha, S., White, G., Woollen, J., Zhu, Y., Leetmaa, A., Reynolds, R., Chelliah, M., Ebisuzaki, W., Higgins, W., Janowiak, J., Mo, K.C., Ropelewski, C., Wang, J., Jenne, R., Joseph, D., 1996. The NCEP/NCAR 40-Year Reanalysis Project. Bull. Am. Meteorol. Soc. 77, 437–471. https://doi.org/10.1175/1520-0477(1996)077<0437:TNYRP>2.0.CO;2
Kaufmann, G., 2003. Stalagmite growth and palaeo-climate: the numerical perspective. Earth Planet. Sci. Lett. 214, 251–266. https://doi.org/10.1016/S0012-821X(03)00369-8
Kim, S.-T., O'Neil, J.R., 1997. Equilibrium and nonequilibrium oxygen isotope effects in synthetic carbonates. Geochim. Cosmochim. Acta 61, 3461–3475. https://doi.org/10.1016/S0016-7037(97)00169-5
Konecky, B.L., Russell, J.M., Rodysill, J.R., Vuille, M., Bijaksana, S., Huang, Y., 2013. Intensification of southwestern Indonesian rainfall over the past millennium. Geophys. Res. Lett. 40, 386–391. https://doi.org/10.1029/2012GL054331
Mühlinghaus, C., Scholz, D., Mangini, A., 2009. Modelling fractionation of stable isotopes in stalagmites. Geochim. Cosmochim. Acta 73, 7275–7289. https://doi.org/10.1016/j.gca.2009.09.010
Novello, V.F., Cruz, F.W., Karmann, I., Burns, S.J., Stríkis, N.M., Vuille, M., Cheng, H., Lawrence Edwards, R., Santos, R. V, Frigo, E., Barreto, E.A.S., 2012. Multidecadal climate variability in Brazil's Nordeste during the last 3000 years based on speleothem isotope records. Geophys. Res. Lett. 39. https://doi.org/10.1029/2012GL053936
Novello, V.F., Vuille, M., Cruz, F.W., Stríkis, N.M., de Paula, M.S., Edwards, R.L., Cheng, H., Karmann, I., Jaqueto, P.F., Trindade, R.I.F., Hartmann, G.A., Moquet, J.S., 2016. Centennial-scale solar forcing of the South American Monsoon System recorded in stalagmites. Sci. Rep. 6, 24762. https://doi.org/10.1038/srep24762
Paterson, D., de Jonge, M.D., Howard, D.L., Lewis, W., McKinlay, J., Starritt, A., Kusel, M., Ryan, C.G., Kirkham, R., Moorhead, G., Siddons, D.P., 2011. The X-ray Fluorescence Microscopy Beamline at the Australian Synchrotron. Struct. Microsc. Appl. Phys. Lett. 1234, 124103. https://doi.org/10.1063/1.3625343
Richey, J.N., Sachs, J.P., 2016. Precipitation changes in the western tropical Pacific over the past millennium. Geology 44, 671–674. https://doi.org/10.1130/G37822.1
Ryan, C.G., Siddons, D.P., Kirkham, R., Dunn, P.A., Kuczewski, A., Moorhead, G., De Geronimo, G., Paterson, D.J., de Jonge, M.D., Hough, R.M., Lintern, M.J., Howard, D.L., Kappen, P., Cleverley, J., Denecke, M., Walker, C.T., 2010. The New Maia Detector System: Methods For High Definition Trace Element Imaging Of Natural Material, in: AIP Conference Proceedings. American Institute of Physics, pp. 9–17. https://doi.org/10.1063/1.3399266
Schulz, M., Mudelsee, M., 2002. REDFIT: estimating red-noise spectra directly from unevenly spaced paleoclimatic time series. Comput. Geosci. 28, 421–426. https://doi.org/10.1016/S0098-3004(01)00044-9
Sinha, A., Cannariato, K.G., Stott, L.D., Cheng, H., Edwards, R.L., Yadava, M.G., Ramesh, R.,

Singh, I.B., 2007. A 900-year (600 to 1500 A.D.) record of the Indian summer monsoon precipitation from the core monsoon zone of India. Geophys. Res. Lett. 34. https://doi.org/10.1029/2007GL030431

Solanki, S.K., Usoskin, I.G., Kromer, B., Schüssler, M., Beer, J., 2004. Unusual activity of the Sun during recent decades compared to the previous 11,000 years. Nature 431, 1084–1087. https://doi.org/10.1038/nature02995

Stuiver, M., Reimer, P.J., Bard, E., Beck, J.W., Burr, G.S., Hughen, K.A., Kromer, B., Mccormac, G., Van Der Plicht, J., Spurk, M., 1998. INTCAL98 RADIOCARBON AGE CALIBRATION, 24,000-0 cal BP 40, 1041–1083. https://doi.org/10.1017/S0033822200019123

Tooth, A.F., Fairchild, I.J., 2003. Soil and karst aquifer hydrological controls on the geochemical evolution of speleothem-forming drip waters, Crag Cave, southwest Ireland. J. Hydrol. 273, 51–68. https://doi.org/10.1016/S0022-1694(02)00349-9

Torrence, C., Compo, G.P., Torrence, C., Compo, G.P., 1998. A Practical Guide to Wavelet Analysis. Bull. Am. Meteorol. Soc. 79, 61–78. https://doi.org/10.1175/1520-0477(1998)079<0061:APGTWA>2.0.CO;2

Vieira, L.E.A., Solanki, S.K., Krivova, N.A., Usoskin, I., 2011. Evolution of the solar irradiance during the Holocene. Astron. Astrophys. 531, A6. https://doi.org/10.1051/0004-6361/201015843

Yamoah, K.A., Chabangborn, A., Chawchai, S., Schenk, F., Wohlfarth, B., Smittenberg, R.H., 2016. A 2000-year leaf wax-based hydrogen isotope record from Southeast Asia suggests low frequency ENSO-like teleconnections on a centennial timescale. Quat. Sci. Rev. 148, 44–53. https://doi.org/10.1016/j.quascirev.2016.07.002

Yan, H., Sun, L., Oppo, D.W., Wang, Y., Liu, Z., Xie, Z., Liu, X., Cheng, W., 2011. South China Sea hydrological changes and Pacific Walker Circulation variations over the last millennium. Nat. Commun. 2, 293. https://doi.org/10.1038/ncomms1297

Yatagai, A., Kamiguchi, K., Arakawa, O., Hamada, A., Yasutomi, N., Kitoh, A., Yatagai, A., Kamiguchi, K., Arakawa, O., Hamada, A., Yasutomi, N., Kitoh, A., 2012. APHRODITE: Constructing a Long-Term Daily Gridded Precipitation Dataset for Asia Based on a Dense Network of Rain Gauges. Bull. Am. Meteorol. Soc. 93, 1401–1415. https://doi.org/10.1175/BAMS-D-11-00122.1

Yoshimura, K., Kanamitsu, M., Noone, D., Oki, T., 2008. Historical isotope simulation using Reanalysis atmospheric data. J. Geophys. Res. 113, D19108. https://doi.org/10.1029/2008JD010074

Zhang, P., Cheng, H., Edwards, R.L., Chen, F., Wang, Y., Yang, X., Liu, J., Tan, M., Wang, X., Liu, J., An, C., Dai, Z., Zhou, J., Zhang, D., Jia, J., Jin, L., Johnson, K.R., 2008. A test of climate, sun, and culture relationships from an 1810-year Chinese cave record. Science 322, 940–942. https://doi.org/10.1126/science.1163965

Zhao, K., Wang, Y., Edwards, R.L., Cheng, H., Liu, D., Kong, X., 2015. A high-resolved record of the Asian Summer Monsoon from Dongge Cave, China for the past 1200 years. Quat. Sci. Rev. 122, 250–257. https://doi.org/10.1016/j.quascirev.2015.05.030